



European Commission

Horizon 2020
European Union funding
for Research & Innovation

E-Infrastructures

H2020-EINFRA-2015-1

EINFRA-5-2015: Centres of Excellence for computing applications

EoCoE

Energy oriented Center of Excellence for computing applications

Grant Agreement Number: EINFRA-676629

D3.4 M36

Application lines: benchmark and results

Project and Deliverable Information Sheet

EoCoE	Project Ref:	EINFRA-676629
	Project Title:	Energy oriented Centre of Excellence
	Project Web Site:	http://www.eocoe.eu
	Deliverable ID:	D3.4 M36
	Lead Beneficiary:	CEA
	Contact:	Edouard Audit
	Contact's e-mail:	edouard.audit@cea.fr
	Deliverable Nature:	Report
	Dissemination Level:	PU*
	Contractual Date of Delivery:	30/09/2018
	Actual Date of Delivery:	30/09/2018
	EC Project Officer:	Carlos Morais-Pires

* - The dissemination level are indicated as follows: PU – Public, CO – Confidential, only for members of the consortium (including the Commission Services) CL – Classified, as referred to in Commission Decision 2991/844/EC.

Document Control Sheet

Document	Title :	Application lines: benchmark and results
	ID :	D3.4 M36
	Available at:	http://www.eocoe.eu
	Software tool:	LaTeX
Authorship	Written by:	U. Aeberhard (Jülich)
	Contributors:	M. Salanne (MdlS), Mario Burbano (MdlS), T. Mendez-Morales (MdlS), Z. Li (MdlS), A. Walker (UBAH), M. Wolf (UBAH), D. Gosh (UBAH), M. Celino (ENEA), S. Giusepponi (ENEA), M. Gusso (ENEA), P. Czaja (Jülich), F. Li (Jülich), U. Aeberhard (Jülich)
	Reviewed by:	PEC members

Document Keywords:
Atomic-scale design, Inorganic Photovoltaics, Perovskite Photovoltaics, Supercapacitors.

Executive Summary:
Application of ab inito MD & DFT to inorganic and perovskite PV, as well as supercapacitors. Link from micro-structural and electronic properties to device functionality. Presentation of results relevant for device performance.

Contents

1 Application line inorganic PV **5**

1.1 Shockley-Queisser analysis 5

1.2 Detailed-balance analysis including optical properties 5

1.3 Assessment including transport - effects of lifetime and mobility 6

1.4 Conclusions 11

2 Application line organic/perovskite PV **12**

2.1 Introduction 12

2.2 Ab initio computational calculations 13

2.3 Drift diffusion simulations 15

3 Application line batteries/supercapacitors **16**

Bibliography **21**

1. Application line inorganic PV

As for any photovoltaic application, the main figure of merit for inorganic PV is the efficiency of conversion of solar power to electrical power, determined as the ratio between the product of current density and voltage at the maximum power point, and the incident radiative power density. In order to assess a given solar cell device from a modelling point of view, different approaches are used, with increasing level of detail on device structure and material properties [1].

1.1 Shockley-Queisser analysis

In the most basic assessment - the famous Shockley-Queisser limit [2] - only the band gap E_{g} of the material is used for the determination of the efficiency. As a consequence, E_g is considered to be the most important material parameter and is usually the first quantity for which potential solar cell materials are screened in high-throughput computations [3]. As experimental data is not available for all of the possible compounds, ab initio methods are required. However, while standard density functional theory based computations of the electronic structure are cheap and fast for simple elemental materials in their crystalline form, such as bulk Si or GaAs, this is no longer the case for compounds with large unit cells and/or strong spin-orbit coupling. Even for the simple cases, there is still the problem of the band gap underestimation of standard DFT, and for a reasonable estimate of the SQ efficiency, more expensive schemes such as hybrid DFT or many-body corrections (GW) need to be applied. In order to estimate the accuracy requirement for the band gap for the SQ analysis, the maximum deviation in the band gap energy allowed to stay within a certain window around the SQ efficiency for the actual band gap can be computed. Figure 1 shows the values of upper and lower errors $\Delta E_g^{\pm}$ for accuracy targets of 1% and 0.1%, respectively, using a 6000 K blackbody spectrum as an approximation for the solar irradiation. As seen in the graphs, the accuracy requirements exceed the capabilities of standard DFT for a wide range of band gap energies, especially in the low and high band gap regimes away from the single junction efficiency peak.

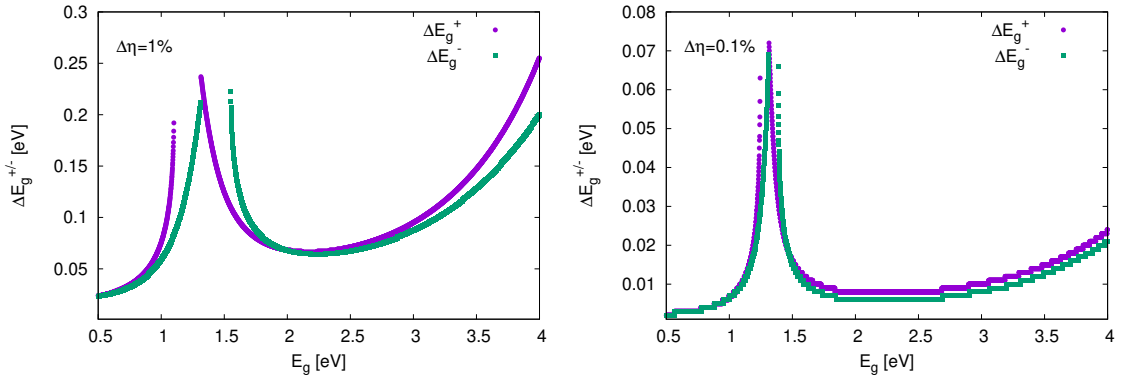


Figure 1: Upper/lower deviation in the band gap value ($\Delta E_g^{\pm}$) allowable to stay within 1% or 0.1% of the corresponding SQ-limit.

1.2 Detailed-balance analysis including optical properties

For a more realistic assessment of the photovoltaic energy conversion efficiency of absorber materials from first principles, the absorption coefficient and the refractive index

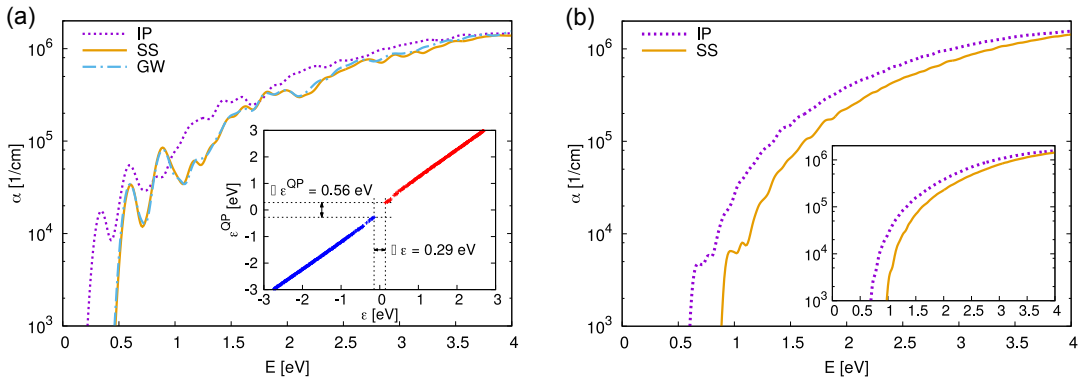


Figure 2: Absorption coefficient of a-Si:H as computed from first principles: (a) 72-atom configuration (64 Si + 8 H) treated in the independent particle approximation (IP) and including many-body corrections (GW); The solid line indicates the fit of the GW result from a scissor shift approach (SS). (b) IP approach and SS correction for the 576 (512 Si + 64 H) configuration; The inset shows a configurational average, where the overestimation of sub-gap contributions is removed. [5]

have to be considered, i.e., the complex dielectric function needs to be computed and used in the analysis [3, 1]. This includes not only the electronic structure, i.e., the available electronic states, but also the matrix elements for optical transitions between these states. In EoCoE, the extraordinary challenging case of hydrogenated amorphous silicon (a-Si:H) was addressed, as it forms an essential part of the silicon heterojunction solar cell which was in the focus of the inorganic PV application line. For that purpose, large a-Si:H supercells with up to 576 atoms were generated via ab initio molecular dynamics and analyzed using density functional theory [4, 5]. Figures 2 (a) and (b) show the absorption coefficient for a-Si:H configurations with 72 and 576 atoms, respectively. Results are shown on the PBE level for the independent particle approximation (IP), with many-body corrections (GW) for the small system, and a GW-fitted scissor shift (SS) for the large configuration. The inset in (b) displays a configurational average that removes the overestimation of the subgap contribution, as the large configuration is on average defect free [5]. As can be inferred from Fig. 2, both many-body and finite size effects play an important role and need thus be considered in a computational characterization approach. However, even for the very large supercell of 576 atoms and including many-body corrections, the experimental band gap of ∼1.6-1.7 eV could not be recovered. This points at a general difficulty in the computational screening of disordered absorber materials, where even very expensive schemes might not satisfy the accuracy requirements established above.

1.3 Assessment including transport - effects of lifetime and mobility

On the next level in the hierarchy of approaches to assess solar cell efficiency, transport needs to be included in order to consider the effects of finite mobility μ and lifetime τ [6]. Conventionally, the associated computational assessment is performed using semi-classical drift-diffusion simulation in combination with generation and recombination rate models obeying the principle of detailed balance [7]. This is a valid approach for solar cell devices that are dominated by the behavior of a bulk absorber material. However, many state-of-the art high-efficiency PV architectures are limited by the carrier dynamics and transport properties in a small number of critical device regions, such as interfaces between absorber components or contacts. Two notable examples are the silicon heterojunction (SHJ) and tunnel oxide passivated contact (TOPCon) solar cell device concepts,

which count among the most promising candidates for the next industrial standard in high-efficiency silicon solar cells, with efficiencies reaching beyond 25% [8, 9]. These device where therefore also in the focus of the EoCoE project, and the main effort was thus in the development of a computational approach to characterize the performance limiting critical hetero-interface regions from first principles, as an essential ingredient for a full multiscale-simulation approach that projects local material properties to global device characteristics [10].

Within EoCoE, two descriptions of the carrier dynamics at the hetero interfaces where developed: an *ab initio* picture starting form the atomistic interface models as reported in deliverable D3.1, and a quantum-kinetic approach based on an effective interface Hamiltonian. Details on both computational approaches are given in deliverable D3.3. Here, we report on the ab initio results relevant for transport and recombination of charge carriers at the interfaces in the SHJ and TOPCon devices introduced above, respectively.

a-Si:H/c-Si interface (SHJ)

The main information relevant for a lowest order assessment of non-radiative carrier lifetime is the density and energetic position of localized defect states in the interface region. In our approach, localized states are identified via their fingerprints in the local density of states (LDOS), atomic coordination and wave function spread, as shown in Fig. 3 for an a-Si:H/c-Si interface configuration with 378 atoms, generated and annealed at room temperature via ab initio MD. In this configuration, there is a large density of sub- and midgap states in the a-Si:H part that can be related to low coordinated atoms and which are strongly localized.

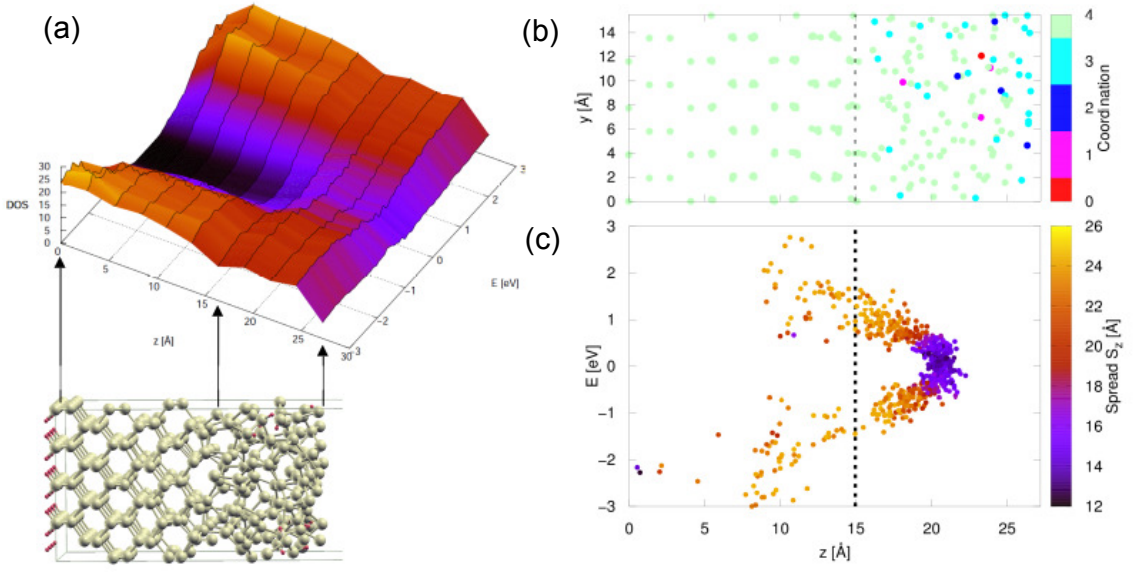


Figure 3: Electronic properties of the a-Si:H/c-Si interface after initial annealing at room temperature: (a) Local density of states (LDOS) exhibiting a large density of recombination-active sub- and mid-gap states; (b) Coordination map for the atoms in the interface region, establishing the connection between midgap defect states and low coordinated atoms in the a-Si:H part; (c) Wave function spread revealing the localized nature of the midgap states in the a-Si:H part. [4]

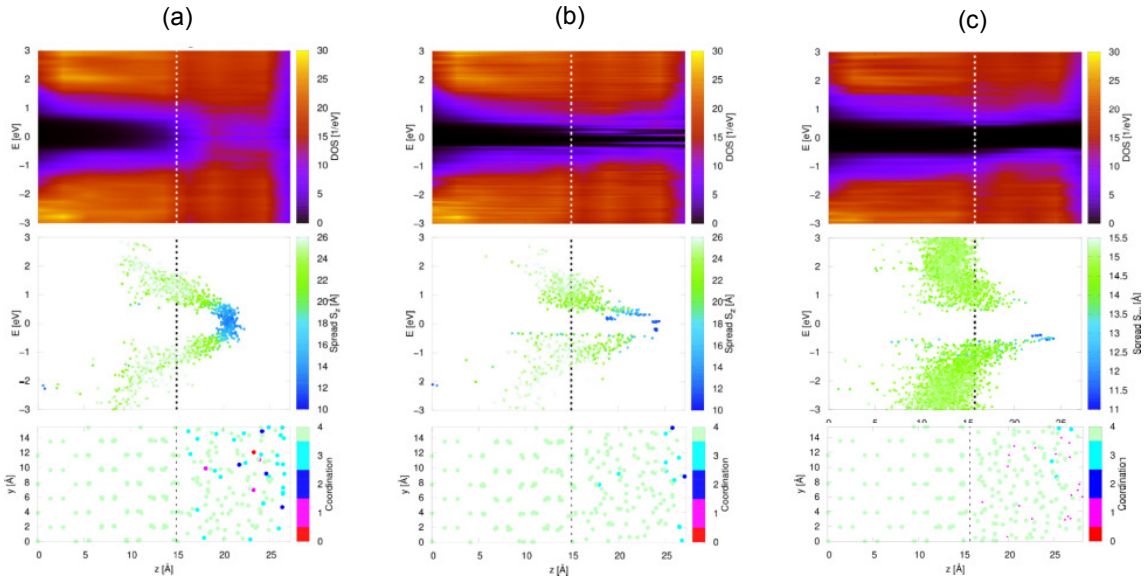


Figure 4: Evolution of the localized recombination-active defect population in the mid-gap energy range as reflected in LDOS, spread and coordination, from (a) the initial configuration after room temperature annealing (25 ps of MD sim.) to (b) the situation after high-temperature annealing (50 ps of MD sim.) and (c) the configuration after an additional surface passivation with hydrogen. [11]

Since the defect density present in this initial configuration is much higher than what is observed experimentally, an additional annealing procedure was applied in the form of 25 ps of MD simulation at elevated temperature. This treatment reduces the defect density significantly, as can be seen in the comparison of the data displayed in Figs. 4 (a) and (b). As strongly localized surface states remain after the thermal treatment, a surface passivation by hydrogen atoms is applied, which clears the gap further [Fig. 4(c)], removing any deep recombination centers.

Regarding transport properties, relevant configurational parameters of the interface to be assessed are the band offsets between crystalline and amorphous phases, especially in the valence band, as holes need to be extracted over this barrier. While the band edges are well defined in the crystalline phase, this is not the case in the amorphous part that contains states with higher localization. Using the sharp threshold in the spread corresponding to extended states evident in c-Si [Fig. 5(a)], a respective transition from localized to extended states can be identified with the mobility gap in a-Si:H [Fig. 5(b)]. The energy thresholds for extended states determined in this way define the band offsets relevant for transport, as visualised in the LDOS and partial DOS in Figs. 5(c) and (d). The ratio of the band offsets for electrons and holes agrees well with experiment, while the absolute values are again underestimated, similar to the situation for the band gap.

In order to relate the electronic structure to the characteristics of charge transport across the interface, quantum transport calculations based on the non-equilibrium Green's function formalism yielding the ballistic conductance are performed using a Wannier-function parametrization as described in deliverable report D3.3. For this purpose, the interface configuration had to be transformed in a sandwich structure with a well defined central scattering region and bulk-like leads, as displayed in Fig. 6(a). This structure was obtained starting from the original interface, attaching the right lead and performing

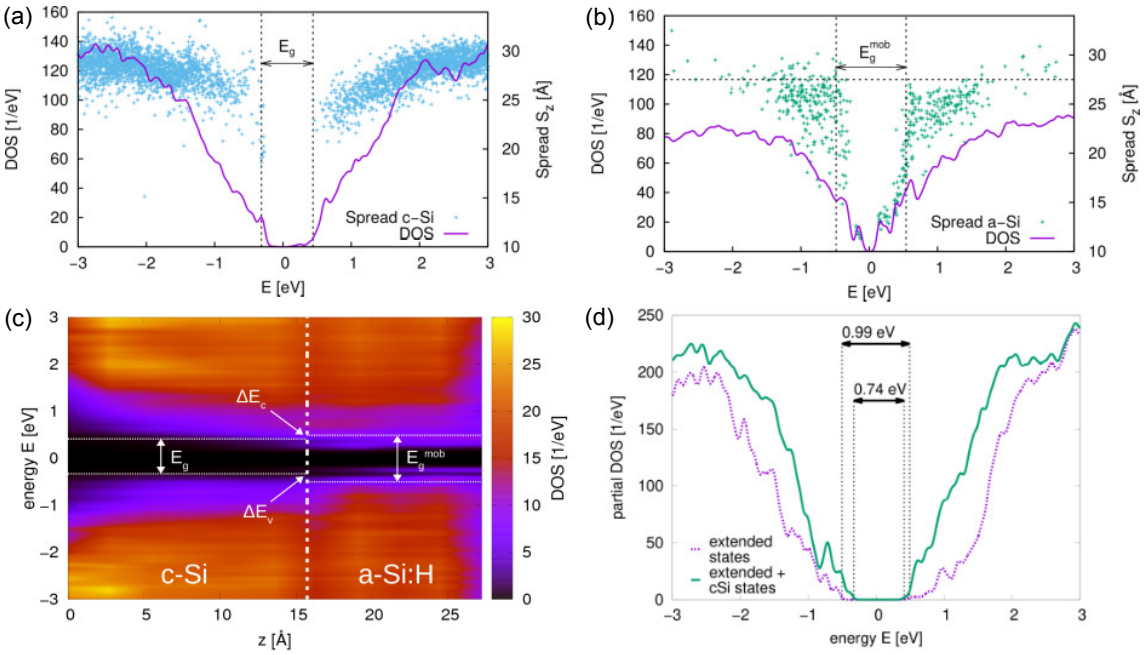


Figure 5: (a) Definition of the band gap of c-Si in terms of the spread for extended states; (b) Definition of the mobility gap following the procedure in (a); LDOS with the band- and mobility edges determined in (a) and (b); (d) Band alignment visualized in the partial DOS. [11]

classical MD using the VASP code. The corresponding LDOS was also computed using VASP on the PBE level, and a good agreement with the QuantumEspresso result displayed in Fig. 5 is found in terms of the band offsets. The quantum conductance displayed in Fig. 6(b) reflects the widening of the mobility gap due to the presence of the a-Si:H layer, while subgap features present in the transmission of the a-Si:H bulk phase are filtered out by the vanishing subgap DOS in the c-Si leads.

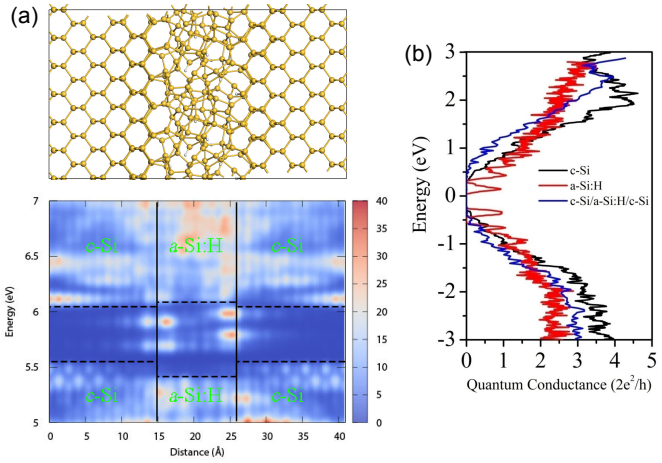


Figure 6: (a) c-Si/a-Si:H/c-Si sandwich structure used for the computation of the conductance, with the corresponding LDOS as computed by VASP given below. (b) Quantum conductance of the sandwich structure, in comparison with the bulk conductances of c-Si and a-Si:H, revealing the widening of the mobility gap and the suppression of a-Si:H subgap features due to vanishing subgap DOS in the c-Si leads.

a-SiOx:H/c-Si interface (TOPCon)

One of the key configuration parameters in the TOPCon architecture is the thickness of the oxide layer, as it needs to be thick enough to spatially separate minority carriers from surface defect states and by this way suppress recombination, and at the same time, tunneling transport should be fast enough to allow for an efficient extraction of majority carriers. In order to study the impact of the oxide thickness from first principles, sandwich structures with oxide layers of 0.6, 0.9 and 1.2 nm thickness were constructed, as displayed in Fig. 7(a). Adjacent to the oxide layers, buffer regions were introduced and relaxed to obtain a more realistic picture of the strain at the c-Si/SiO_x interface. Indeed, as shown in the LDOS maps in Fig. 7(b), there are surface states in the gap, at an energetic position that depends on thickness. More importantly, however, there is a strong decrease of the DOS in the barrier with increasing thickness, which translates to a pronounced drop of conductance [Fig. 7(c)]. An additional feature evidenced in Fig. 7(c) is the asymmetry between electron and hole conductance, which can play a role for the selectivity of the contact.

Since recombination of carriers at defects competes with carrier extraction, passivation with hydrogen is considered also in this case, as illustrated in Fig. 8(a) for the example of a surface defect. The LDOS map in Fig. 8(b) shows successful removal of some of the defects states in the gap by the hydrogen treatment, while other deep states persist, but are energetically shifted out of the detrimental mid-gap position. In the conductance displayed in Fig. 8(c), the modification due to hydrogen shows up in the form

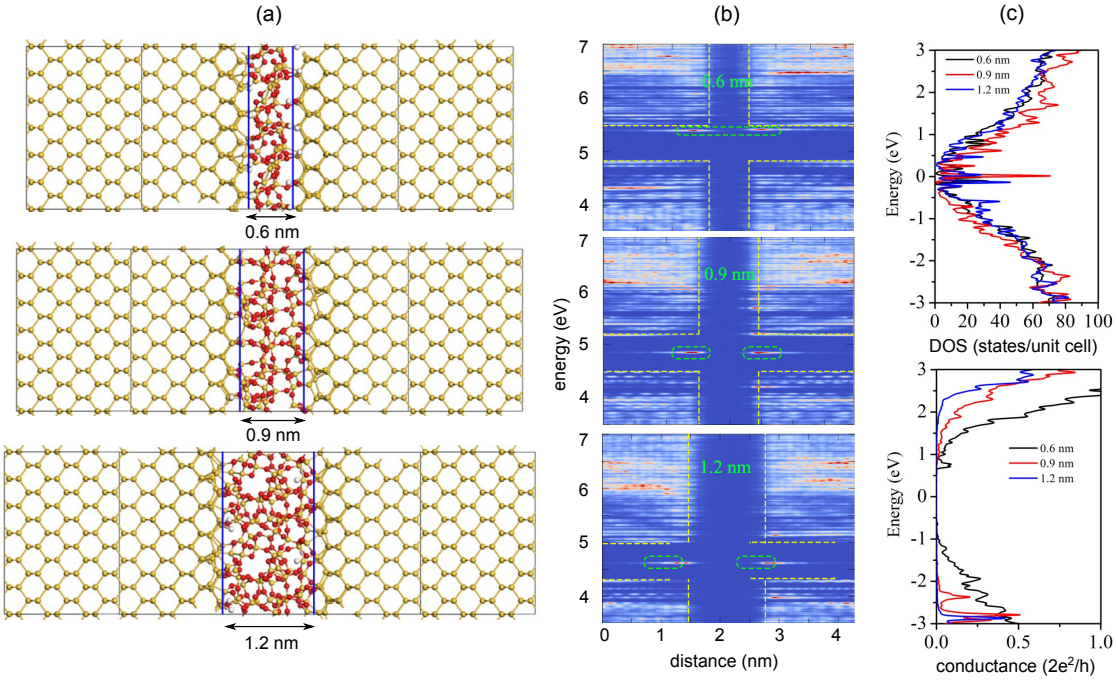


Figure 7: (a) c-Si/SiO_x/c-Si sandwich structures with oxide thickness of 0.6, 0.9 and 1.2 nm; (b) Corresponding LDOS, revealing the presence of thickness-dependent surface states and the strong decrease of the DOS in the barrier with increasing thickness; (c) Spatially integrated DOS and conductance for the three structures. The conductance shows the strong suppression of transport with increasing thickness as well as the asymmetry of electron and hole transport. [12]

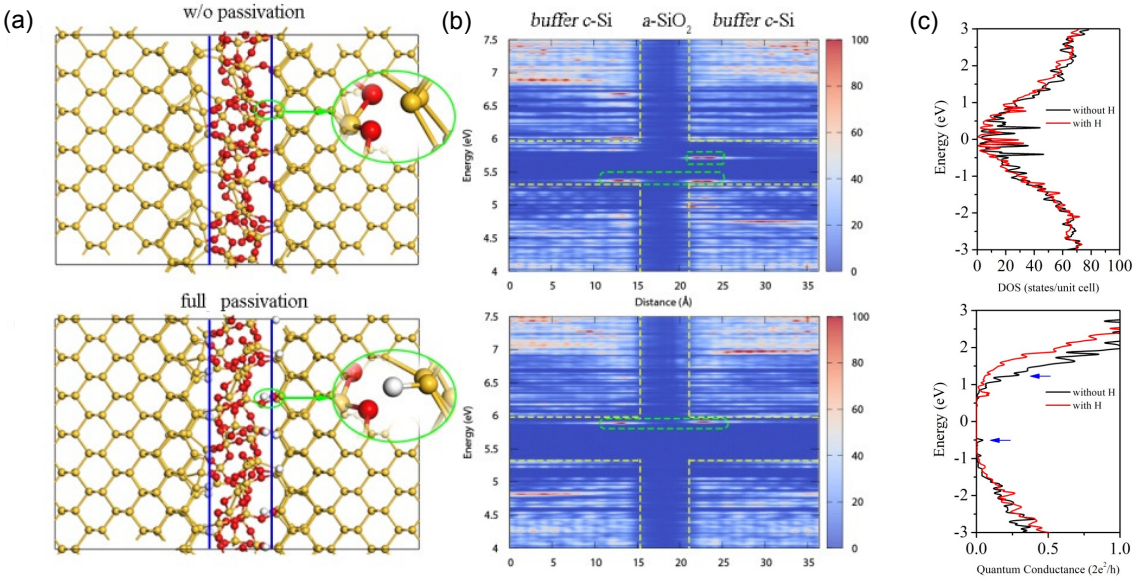


Figure 8: (a) Hydrogen passivation of interface defects; (b) LDOS of unpassivated and passivated structures, revealing the removal and energetic shift of defect states upon hydrogen treatment; (c) Modification of DOS and conductance due to hydrogen passivation: While the DOS in the gap is reduced, conductance is not only suppressed due to removal of conductance channels, but also at higher energies. [12]

of the removal of defect mediated transmission channels, but also an unexpected decrease of electron conductance at higher energies is observed.

Since the dramatic reduction of conductance with oxide thickness displayed in Fig. 7(c) is in contrast to the experimentally observed optimum thickness of ∼1 nm [13], direct tunneling alone is not likely to be sufficient to explain transport through the oxide. We therefore investigated the impact of oxygen vacancy defects on the conductance of the thick (1.2 nm) barrier layer. Single defects were positioned both at the surface and in the bulk of the oxide, and chains with increasing number of vacancies were considered as well. Remarkably, as a common feature observed in all cases, the oxygen vacancies are unstable and recombine forming a new (strained) silicon bond. For multiple vacancies, a silicon chain is formed, which for a number of defects greater than four creates a mono-filament pin-hole connecting the c-Si buffer layers [Fig. 9(a)]. While single defects are barely detectable in the LDOS, the silicon chain creates a continuous DOS in the gap. As indicated by the LDOS picture, there is only marginal impact of single defects on the conductance, irrespective of the defect location, while the mono-filament pin-holes drastically increase the transmission and hence offer an alternative explanation for the experimentally observed levels of conductance.

1.4 Conclusions

In conclusion, performance critical aspects of the industrially relevant silicon technologies based on a-Si:H/c-Si heterointerfaces and a-SiO_x:H/c-Si tunnel contacts were investigated from first-principles, using a combination of ab initio MD, DFT and Green's function transport methods. For the SHJ concept, microscopic relations between defect density and mobility gap were established, and interface structures that are in qualitative agreement with experimental observations in terms of defects density and band offsets were obtai-

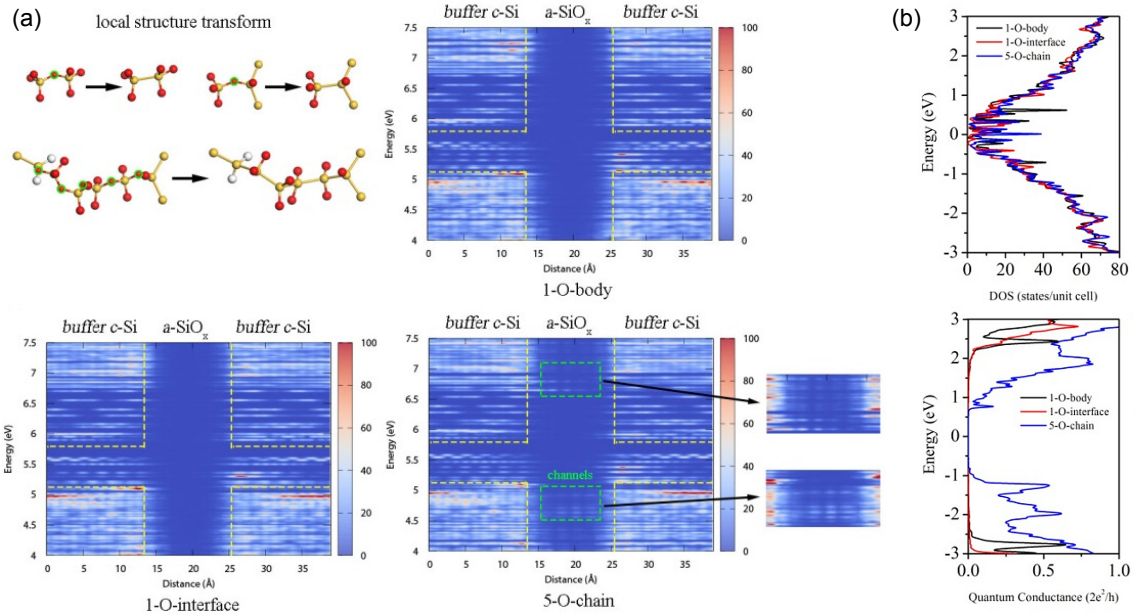


Figure 9: (a) Structural modification induced by the introduction of single or multiple oxygen vacancies at the surface or in the bulk of the oxide layer. While single defects are barely detectable in the LDOS, chains of multiple defects create new transport channels bridging the gap induced by the barrier; (b) The impact of single defects on the conductance is marginal, irrespective of the location of the defects, while the formation of a silicon chain due to recombination of multiple vacancies drastically increases the conductance for both electrons and holes. [12]

ned. However, quantitative agreement remains a challenge for this material system. For the TOPCon architecture, transport enhancement due to the formation of mono-filament pin-holes by recombination of oxygen vacancies in the oxide barrier was identified as a mechanism that could explain the conductivity levels observed experimentally for oxide thicknesses where transport via direct tunneling is inefficient.

2. Application line organic/perovskite PV

2.1 Introduction

Perovskite solar cells, PSC, have attracted huge interest since 2012 through fast rising power efficiencies, PCEs, now comparable to Si cells. For example PSC/Si tandem cells reported PCEs in June 2018 of 27.3% [14], exceeding the 26.7% efficiency world record for a single-junction Si solar cell. The light harvesting layer in PSCs is a semiconductor with the perovskite structure. An example structure taken from reference [18] is shown in Figure 10. However, the structural changes at the atomic scale and modifications to the optoelectronic properties of these mixed cation perovskites are not fully understood. In this deliverable, UBAH reports on studies of (i) structural distortions by a combination of static and dynamic ab initio computational methods that have implications for transport processes in bulk perovskites and (ii) mixed ion-electron conduction by a drift diffusion model that obtains PSC characteristics for different cell architectures and reverse engineers the characteristics to find activation energies for ion vacancy motion. These results, listed in inverse chronological order in references [15]–[22] have been published or are under

review. EoCoE funded authors are underlined. Most of these papers include experimental results reported for the first time made by groups mainly at UBAH.

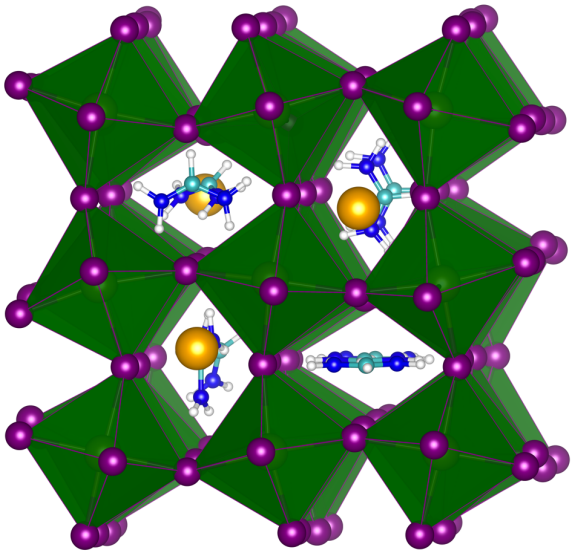


Figure 10: Schematic structure of a mixed A-cation metal halide perovskite. The A cations, FA^+ and Cs^+, occupy the inorganic cavity formed by corner-sharing PbI_6 octahedra (green). Key: iodine (purple), hydrogen (white), carbon (cyan), nitrogen (blue), caesium (orange).

2.2 Ab initio computational calculations

These methods are described with a full set of citations in the supplementary information for [22]. In brief, well-established ab initio molecular dynamics (AIMD) techniques were used [23] The mixed halide perovskites were modelled using a large supercell, up to $4 \times 4 \times 4$ (containing 768 atoms) in size, which enabled us to resolve doping levels to better than 2% and to provide a good statistical sample size for the dynamics. Compositions representative of those reported experimentally in [15]–[22] were considered by for example substituting new cation species for FA^+. For each composition, various ordered configurations of the A-site species were considered, and the lowest energy structure was selected.

We performed AIMD simulations at a temperature of 300 K using the CP2K code [24]. The QUICKSTEP formalism was employed where the Kohn-Sham orbitals were expanded in an atom centred DZVP Gaussian basis sets and the electronic charge density in an auxiliary plane wave basis sets with a 300 Ry energy cutoff. Analytical dual-space pseudopotentials and the generalised gradient approximation with the Perdew-Burke-Ernzerhof functionals for solids (PBEsol form) were used. Additionally, we applied van der Waals interactions. Inclusion of spin-orbit coupling has an insignificant effect on the geometry of lead iodide perovskites and we have not included it in our AIMD simulations. Each simulation covered a time period of 12 ps with a timestep of 1 fs. These systems take 2–3 ps to reach equilibrium and so we used the final 9 ps for analysis. Equilibrium dynamics were maintained in the NPT ensemble using a Nose-Hoover thermostat and a barostat.

Reference [22] addresses hybrid lead halide perovskites containing a mixture of A-site cations such as methylammonium (CH_3NH_3, MA) formamidinium ($CH(NH_2)_2$, FA) and the smaller cesium (Cs^+) cations that have attracted considerable interest due to

their improved stability and solar cell performance. We show that substitution of low concentrations of smaller cations on the A-site in $FAPbI_3$ results in a global locking of the PbI_6 octahedra tilting. In the locked structure the octahedra tilt at a larger angle but undergo a much reduced amplitude of rocking motion. A key impact of this feature is that the rotational or tumbling motion of the FA molecular ion in a locked cage is severely restricted. These structural changes are significant as the electronic band gaps, relevant to photovoltaic behaviour, are associated with Pb–I bond hybridisation. Our study indicates that the bond angle and therefore the band gap will undergo much smaller fluctuation and result in more monochromatic light absorption profile in the mixed A-site cation perovskite systems. This reduced electronic disorder is the most likely reason for recently observed increased charge mobilities in these mixed-cation systems.

In [20], ab initio calculations were performed using density functional theory (DFT) implemented in the Vienna Ab initio Simulation Package (VASP 5.3.5)6. In order to construct the plane-wave basis-set, a cut-off of 500 eV was used. Ion-electron interactions were included by employing the projected augmented wave (PAW) method. Generalized gradient approximations (GGA) in the form of PBEsol capture the exchange-correlation interactions. Although GGA-PBEsol functionals underestimate the absolute band-gap of hybrid perovskites, they successfully reproduce the trend in band-gap values for similar mixed perovskites. To describe the band-dispersion, spin-orbit coupling (SOC) was included for valence electrons for the band structure calculations.

We show that it is possible to make mixed cation devices by adding the azetidinium cation $[(CH_2)_3NH_2]^+$, AZ) to lead iodide [21]. UBAH computational studies find that the substitution of up to 5% Az^+ into $MAPbI_3$ is energetically favourable and that phase separation does not occur at these concentrations. Mixed AZ–MA cells are found to have improved performance and reduced hysteresis compared to $MAPbI_3$ cells.

Lead-free perovskites based on germanium and tin solid solutions, $MASn1-xGe_xI_3$ ($0 \leq x \leq 1$) were fabricated and characterized [20]. We show that these perovskite compounds possess band gaps from 1.3 to 2.0 eV, which are suitable for a range of optoelectronic applications, from single junction devices and top cells for tandems to light-emitting layers. The UBAH contribution is calculation of their thermodynamic stability and electronic properties for all compositions that agree well with the reported experimental measurements. Our findings demonstrate an attractive family of lead-free perovskite semiconductors with a favourable band-gap range for efficient single-junction solar cells

The low-temperature phases of $FAPbI_3$ were investigated using rapid neutron powder diffraction in [19]. AIMD studies were made by UBAH of cation reorientation over the same temperature range, which indicate contrasting FA motion in the cubic and tetragonal structures. We see complete disorder of the FA cations in the cubic phase at 300 K. The PbI_6 octahedra also undergo periodic tilting oscillations which on average produce the pseudocubic structure. These structural dynamics indicate weak lattice?cation coupling between the organic cations and inorganic framework. In contrast, for the mid-temperature tetragonal β–phase there is restricted motion of the FA^+ cation with preferred orientations within the A-site cage.

The most recent published paper at the time of this deliverable, [18], is a solely theory paper showing that the incorporation of Cs^+ cations into the parent $FAPbI_3$ structure induces a chemical pressure or lattice strain effect through Cs/FA ion size mismatch resulting in structural distortion and stronger FA-iodide (N–H–I) hydrogen bonding inte-

ractions. The dynamic tilting of PbI_6 octahedra and the rotational motion of FA cations are also suppressed, which leads to symmetry-breaking of the lattice. Such symmetry-breaking distortions of the Pb/I lattice give rise to a Rashba-type effect, which spin-splits the frontier electronic bands making the band gap indirect. Our results suggest that the direct?indirect band gap transition may be a factor in the reduced charge-carrier recombination rate in these mixed cation perovskites.

A publication under review, [15], is a joint experimental-theory paper with authors from UBAH and an author from the UK ISIS Neutron & Muon Source. For the first time, we reveal the effect on iodide ion transport of incorporating small levels of six different sized cations from small Cs^+ to large guanidinium, ($CH_6N_3^+$, GA). The results obtained from experiment and simulation show strong agreement, indicating that (see Figure 11) all the cation substitutions increase the activation energy for iodide ion transport relative to pure $MAPbI_3$. Just 5% GA substitution strongly supresses iodide ion transport, with no observable ion diffusion in the timescale of our measurements. This combined study enhances our fundamental understanding of mixed-cation perovskites, and provides a design strategy for reducing iodide ion transport that has important implications for improving solar cell performance demonstrated in the drift diffusion simulations described in the following subsection.

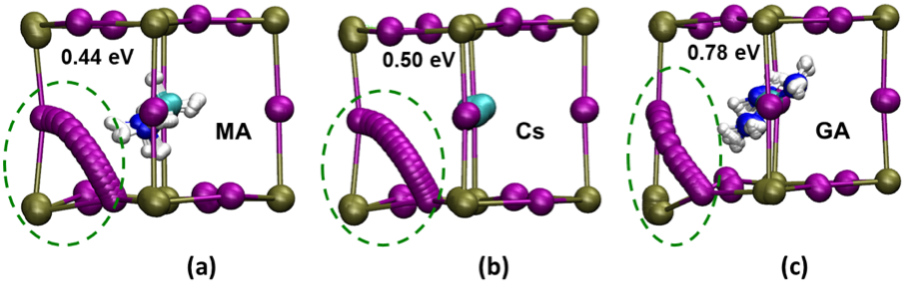


Figure 11: Ab initio simulations of the ion transport paths, the activation energies and the lattice ion displacements in (a) $MAPbI_3$ (b) $MA_{0.75}Cs_{0.25}PbI_3$ and (c) $MA_{0.75}GA_{0.25}PbI_3$. (Key: Pb, green; I, purple.) Local lattice relaxations near the diffusion path are highlighted by green circles, showing greater structural distortion in the GA-substituted material.

2.3 Drift diffusion simulations

We investigated PSCs employing $MAPbI_3$, $FAPbI_3$ and $MAPbBr_3$ [16] Electron transport layers are SnO_2 or TiO_2 and hole transport layers spiro-OMeTAD, 2,2',7,7'-tetrakis[N,N-di(4-methoxyphenyl)amino]-9,9'-spirobifluorene (spiro). Halide vacancy motion is widely accepted as a cause of efficiency loss, degradation and anomalous current-voltage hysteresis in PSCs. The variation of cell current-voltage, $J-V$, characteristics and amount of hysteresis on temperature, measurement speed and architecture are investigated for four solar cell structures with varying materials compositions. These measurements in combination with a coupled charge transport model for electron, hole and ion motion [16, 17], show that ion motion reduces cell performance even when operating at steady state. The current-voltage scan rate exhibiting maximal hysteresis offers an estimate of the timescale of ion motion in the perovskite layer as shown in Figure 12. The hysteresis factor $H = (A_{\rm rev} - A_{\rm for})/A_{\rm rev}$, where $A_{\rm rev}$ and $A_{\rm for}$ are the areas under the reverse and forward scan respectively. From its temperature variation, we deduce activation energies for halide

ion motion that compare well with Density Functional Theory calculations. We argue that a large body of work on perovskite cells should be reassessed. For example, from 2017 to now, a Google Scholar search for "hysteresis-free" cells that have architectures and materials compositions lists almost 1,000 items. We question the extent to which these devices really are hysteresis free and show that there are implications for the steady state performance of devices that show hysteresis. Also, we quantify the extent to which hysteresis depends on the scan rate. Many reports of current-voltage curves do not state the scan rate so the interpretation of their results is ambiguous.

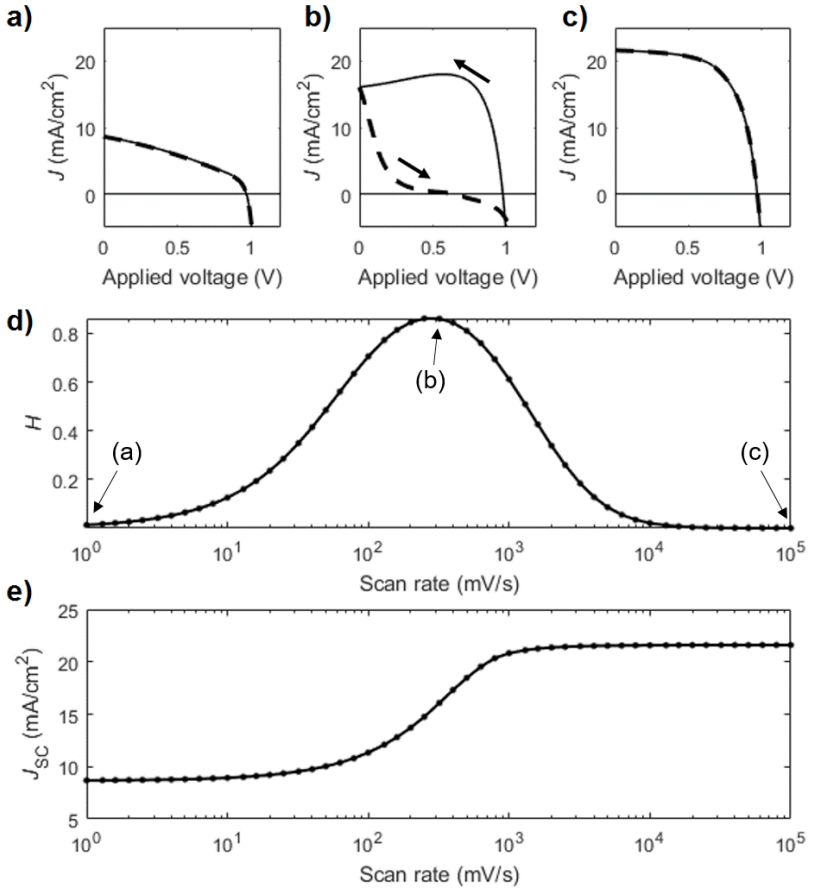


Figure 12: Panels (a)-(c) Simulated $J-V$ curves for a planar SnO_2/MAPI/spiro device with scan rates of (a) 1 mV/s, (b) 320 mV/s and (c) 100 V/s at 315 K. Solid lines indicate the reverse scan and dashed lines the forward scan The result of the model when ions are fixed is essentially identical to the 100 V/s scan in panel (c); without moving ions there is no dependence on scan rate, and no hysteresis. (d) Hysteresis factor H as a function of scan rate. (e) Measured short circuit current as a function of scan rate.

3. Application line batteries/supercapacitors

Carbon-based supercapacitors are electrochemical devices that store electricity through the adsorption of ions from an electrolyte at the surface of porous electrodes. For decades, the state-of-the-art materials for the latter were mesoporous, *i.e.* with pore sizes ranging from 2 to 50 nm [25]. In this family of materials, the capacitance, which quantifies the

charge stored in the electrode as a function of applied voltage, was generally correlated with the accessible surface area (ASA): the larger the surface, the larger the capacitance. Thus the relative performances of carbon materials were usually compared by normalizing the capacitance with the ASA. This allowed for example to address the effect of various activation techniques after synthesis.

The use of microporous carbons (with pore sizes distributed below 2 nm) [26, 27] has deeply impacted this field of research [28]. It was then shown that the capacitance per unit surface area could be greatly enhanced while keeping the ASA relatively constant, suggesting that other physico-chemical features play an important role. The matching between the pore size and the ionic dimensions was quickly identified as a key aspect [29], and although this picture has now been refined through the use of various theoretical [30, 31], simulation [32, 33] and *in situ* experimental techniques [34], it is now widely accepted that the pore size distribution (PSD) of the carbon materials is playing a role of utmost importance [35].

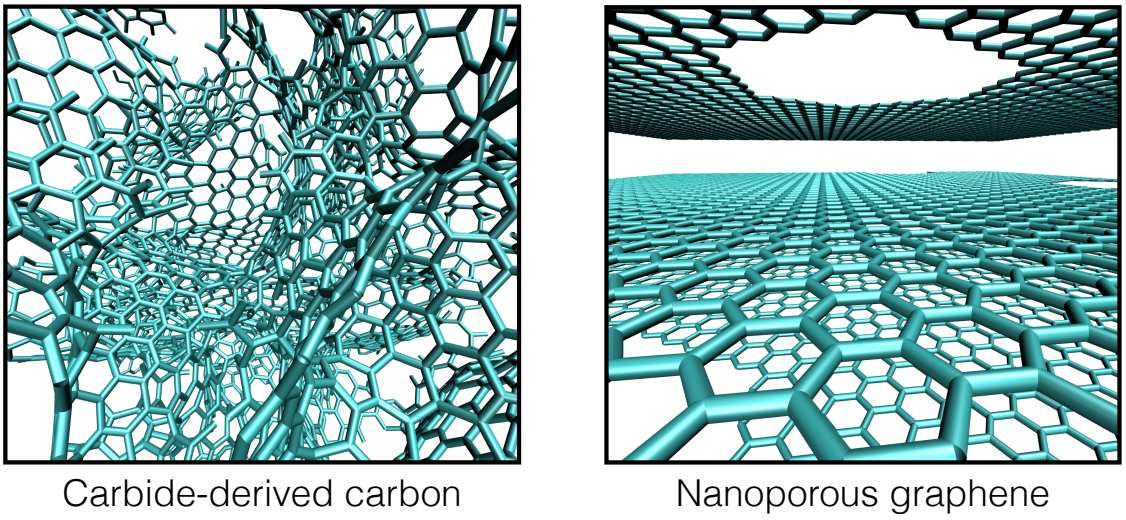


Figure 13: Representative snapshots of the inner structure of the two nanoporous carbon electrodes simulated in this study. In the graphene case, the interlayer spacing is systematically varied between 7 and 10 Å.

However, despite these advances, it is still very difficult to predict the performance of a carbon material solely based on its ASA and/or its PSD. In fact, even the experimental determination of these quantities should be subject to caution in micropores. As a consequence, it remains necessary to perform lengthy electrochemical testings. This is particularly true for comparing carbons with very different textures. It would therefore be highly desirable to develop accurate simulation methods that allow to determine the capacitance and to link it to the microscopic charging mechanisms. Here we illustrate this by simulating two types of nanoporous carbons with very different features using molecular dynamics. As shown on representative snapshots on 13, the first system consists in a carbide-derived carbon (CDC) with a highly disordered structure. It was obtained by Palmer *et al.* [36] using quenched molecular dynamics and was shown to match with an experimental structure of a CDC synthesized at 1,200°C (it will be labelled CDC-1200 in the following). We compare it to a series of highly-ordered nanoporous perforated graphene (PG) electrodes consisting of 6 graphene planes separated by an interlayer distance which was systematically varied between 7 and 10 Å. Holes were included inside the structure to allow the access of the

ions (the full details of the simulations are provided in the supplementary information). The electrolyte is a pure ionic liquid, the 1-butyl-3-methylimidazolium hexafluorophosphate, which is modelled using a coarse-grained description [37] which was validated in the context of electrochemical cells in our previous works [38, 39]. Full supercapacitors are simulated by setting up symmetric cells in which the electrolyte is put in contact with two similar electrodes. The latter are polarized through the application of a constant potential difference between them. In order to discuss comparable state-of-charges for all the systems, we equilibrate them by fixing the charge on each carbon atom to 0.01 e. Then we apply a series of potential $\Delta\Psi$ in short simulations, until we find a value for which there is no drift in the total charge of the electrode. During this production step the individual charges carried by the carbon atoms are allowed to fluctuate [40]. This leads to values of 1.0 V (CDC-1200), 1.8 V (graphene with interlayer spacings of 7, 8 and 9 Å) and 2.7 V (graphene with interlayer spacing of 10 Å). The molecular dynamics simulations are made with a time step of 2 fs for integrating the equations of motion, and trajectories of 1.3 ns are accumulated.

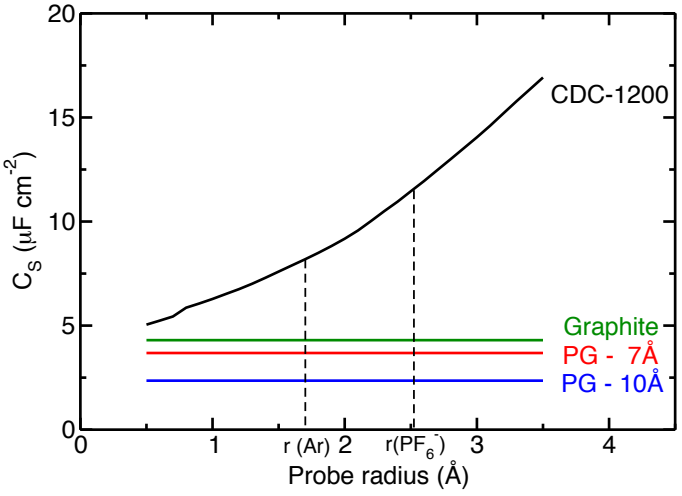


Figure 14: The ASA is not a well defined quantity for comparing the performances of materials with different pore size distributions and surface topologies. Surfacic capacitance of the various nanoporous carbon materials are shown depending on the size of the probe used to calculate the ASA. The value for graphite is also provided for comparison.

The (non-normalized) capacitance of the simulated supercapacitor is given by

$$C = \frac{\langle Q_+ \rangle}{\Delta\Psi} \tag{1}$$

where $\langle Q_+ \rangle$ is the average charge of the positive electrode over the full simulation. However, this quantity cannot be compared directly between systems since the CDC and the nanoporous graphenes have different ASA, mass and volume. In a first step, we try to normalize it by calculating the ASA. In principle, this should more easily be done in simulations than in experiments since we have access to the exact molecular structure. We use the software Zeo++ [41, 42], in which the only required parameter is a probe size. The ASA was systematically determined for sizes ranging between 0.5 and 3.5 Å, which encompass the estimated values for the probes used in adsorption experiments (such as Argon) and for the ions of our electrolyte. It is immediately seen on 14 that whatever the probe, the CDC always outperforms the PGs. If we limit the comparison to the Argon

and the PF_6^- radii, the CDC surfacic capacitance is largest by factors of 2.2 and 3.1 than the one of the best performing PG (with 7 Å interlayer distance). This result is somewhat unexpected since the latter geometry is supposed to give the best access to the surface while ensuring that the ionic dimensions match with the pore size. However, if we also compare with the case of graphite, for which only one side of the carbon plane is accessible to ions, we immediately see that the capacitance per unit surface area is also higher than the ones of perforated graphenes.

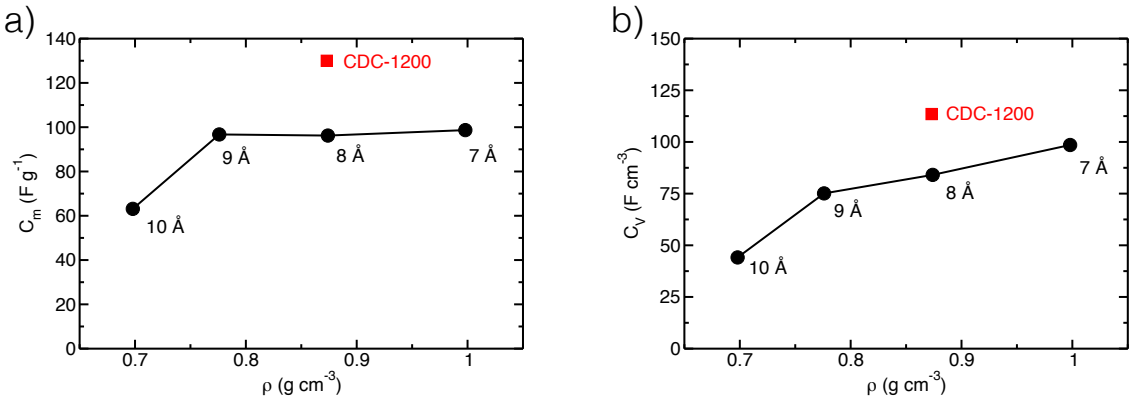


Figure 15: Materials performance. The capacitance normalized by the electrode mass (panel a) or volume (panel b).

Before analyzing the origin of these differences in performance at the microscopic scale, it is useful to do additional comparisons with less probe-dependent normalizations, which can be done by computing the specific and volumetric capacitances (normalization by the mass and the volume of the electrode, respectively). As shown on 15, in both cases the CDC-based supercapacitor remains the most performant, even though the difference is much less pronounced than when using the ASA for the normalization. The specific capacitance is 30 % larger (130 F g^{-1} in CDC-1200 compared to 100 F g^{-1} in the nanoporous graphene with pore sizes ranging between 7 and 10 Å). As for the volumetric capacitance (panel b), taking profit from the shorter distance between the planes and consequently its high density, the 7 Å PG almost reaches the same value as the CDC (99 F cm^{-3} compared to 112 F cm^{-3}).

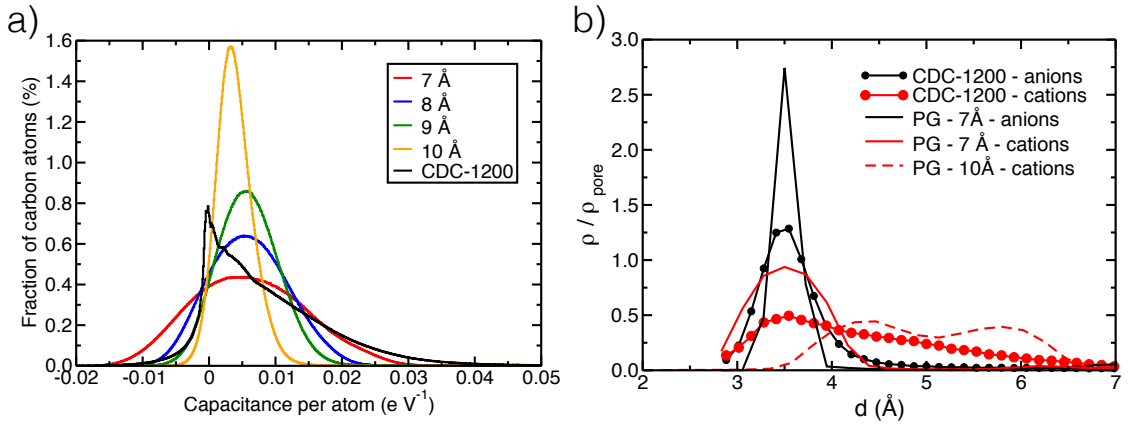


Figure 16: Interpretation of the performances of the materials. a) Distributions of capacitances per atom are given for all the positively charged electrodes. b) Ion density profiles normal to the positive electrode surface for various CDC and PG materials (normalized by the total density of the pore).

In order to estimate the effect of the local structure on the capacitance, we compute the distribution of capacitance per carbon atom for a positively charged electrode, defined as $q_i/\Delta\Psi$, where q_i is the local charge carried by a carbon atom, in 16a). Firstly, we observe that the distribution is much more skewed for the CDC than for all the nanoporous graphene electrodes, in agreement with our previous work [38]. However the 7 Å wide nanoporous graphene shows a broad distribution, with a relatively large number of highly charged carbon atoms. The reason for its lowest performance is therefore to be found in the negative side of the distribution. Contrarily to the CDC, which almost has no negatively charged carbon, the 7 Å distribution exhibits the largest numbers among all the studied electrodes. This is due to the peculiar geometry of the nanoporous graphenes. Since there is only one pore size, anions and cations necessarily lie in the middle of the pore. As shown in our recent study focusing on the structure of the liquid, a monolayer of ions is formed for separations ranging between 7 and 9 Å, but in the 10 Å this monolayer is split in two, leading to two subpeaks with smaller intensities [43]. Therefore the cations that still remain inside the pores are very close to the carbon surface and are therefore at the origin of the observed large negative charges in the 7 Å nanoporous graphene. In the CDC electrode, the structure is very different: There are several pore sizes within the material (ranging from 7 Å to 10 Å), which allows strong reorganizations of the liquid structure. As a consequence, cations tend to move away from the surface and to reside in the middle of the largest pore, so that they do not induce negative charges on the carbon atoms.

This analysis is further corroborated by computing the ionic densities inside the pores, with respect to the distance to the pore wall. As shown in 16b for the positively charged electrode, where they are normalized by the total pore density for each species, the distribution of anions is qualitatively similar in the CDC-1200 and the 7 Å PG. On the contrary, while in the graphene the cations share the same layer as the anions (leading to a distribution centered at the same distance to the electrode as for the anions), in the CDC-1200 the cation distribution is much broader, with some surface-cation distances reaching similar values as in the 10 Å nanoporous graphene.

In conclusion, molecular dynamics simulations allow to directly compare the performance of a variety of electrode structure at the same level of description and without the various sources of discrepancies that may be found in experiments (presence of surface groups in the carbons, discrepancies linked to the difficult characterization of nanoporous structures). In this work, by comparing a disordered nanoporous carbon with regular structures made of perforated graphene layers with various interlayer spacings, all of them put in contact with the same ionic liquid, we were able to show the importance of allowing co-ions (i.e. ions of the same sign as the electrode) to adopt positions far from the surface in order to maximize the capacitance. This result reinforces the idea that hierarchical nanoporous structures are potential good candidates for supercapacitor applications, not only for allowing a faster diffusion of the ions but also for increasing the capacitance – on the contrary too narrow pore size distributions should probably be avoided.

Although these findings may be generalized to the case of organic electrolytes for supercapacitors (since they generally charge with similar mechanisms as ionic liquids [44]), further investigation should be performed in the case of aqueous solutions. The latter, which are used for blue energy / desalination applications [45], involve inorganic ions that are difficult to desolvate, even in nanopores [46], which may impact strongly on the structure of the liquid inside perforated graphene electrodes.

References

[1] Uwe Rau, Beatrix Blank, Thomas C. M. Müller, and Thomas Kirchartz. Efficiency potential of photovoltaic materials and devices unveiled by detailed-balance analysis. *Phys. Rev. Applied*, 7:044016, 2017.

[2] William Shockley and Hans J. Queisser. Detailed balance limit of efficiency of p-n junction solar cells. *J. Appl. Phys.*, 32(3):510–519, 1961.

[3] Liping Yu and Alex Zunger. Identification of potential photovoltaic absorbers based on first-principles spectroscopic screening of materials. *Phys. Rev. Lett.*, 108:068701, 2012.

[4] Philippe Czaja, Massimo Celino, Simone Giusepponi, Michele Gusso, and Urs Aeberhard. *Ab Initio Description of Optoelectronic Properties at Defective Interfaces in Solar Cells*, pages 111–124. Springer International Publishing, Cham, 2017.

[5] Philippe Czaja, Massimo Celino, Simone Giusepponi, Michele Gusso, and Urs Aeberhard. Ab initio study on localization and finite size effects in the structural, electronic, and optical properties of hydrogenated amorphous silicon. *Computational Materials Science*, 155:159 – 168, 2018.

[6] Uwe Rau. Reciprocity relation between photovoltaic quantum efficiency and electroluminescent emission of solar cells. *Phys. Rev. B*, 76(8):085303, 2007.

[7] Thomas Kirchartz and Uwe Rau. Detailed balance and reciprocity in solar cells. *physica status solidi (a)*, 205(12):2737–2751, 2008.

[8] Kunta Yoshikawa, Hayato Kawasaki, Wataru Yoshida, Toru Irie, Katsunori Konishi, Kunihiro Nakano, Toshihiko Uto, Daisuke Adachi, Masanori Kanematsu, Hisashi Uzu, and Kenji Yamamoto. Silicon heterojunction solar cell with interdigitated back contacts for a photoconversion efficiency over 26%. *Nature Energy*, 2:17032, 2017.

[9] Armin Richter, Jan Benick, Frank Feldmann, Andreas Fell, Martin Hermle, and Stefan W. Glunz. n-type si solar cells with passivating electron contact: Identifying sources for efficiency limitations by wafer thickness and resistivity variation. *Solar Energy Materials and Solar Cells*, 173:96 – 105, 2017. Proceedings of the 7th international conference on Crystalline Silicon Photovoltaics.

[10] Urs Aeberhard, Philippe Czaja, Markus Ermes, Bart E. Pieters, Ganna Chistiakova, Karsten Bittkau, Alexei Richter, Kaining Ding, Simone Giusepponi, and Massimo Celino. Towards a multi-scale approach to the simulation of silicon heterojunction solar cells. *J. Green Engineering*, 5:11–32, 2016.

[11] Philippe Czaja, Simone Giusepponi, Michele Gusso, Massimo Celino, and Urs Aeberhard. Computational characterization of a-Si:H/c-Si interfaces. *Journal of Computational Electronics*, OnlineFirst, 2018.

[12] Feng Li, Weiyuan Duan, Philippe Czaja, Manuel Pomaska, Kaining Ding, Uwe Rau, and Urs Aeberhard. Quantum transport across amorphous-crystalline interfaces in Tunnel-Oxide Passivated Contact solar cells: direct vs.defect-assisted tunneling. In preparation, 2018.

[13] Malte Köhler, Manuel Pomaska, Florian Lentz, Friedhelm Finger, Uwe Rau, and Kaining Ding. Wet-chemical preparation of silicon tunnel oxides for transparent passivated contacts in crystalline silicon solar cells. *ACS Applied Materials & Interfaces*, 10(17):14259–14263, 2018.

[14] M. Peplow. Perovskite progress pushes tandem solar cells closer to market. Chem & Eng. News, 96, 2018.

[15] D. W. Ferdani, Samuel R. Pering, D. Ghosh, P. Kubiak, A. B. Walker, S. E. Lewis, A. L. Johnson, P. J. Baker, M. S. Islam and P. J. Cameron. Partial Cation Substitution Reduces Iodide Ion Transport in Lead Iodide Perovskite Solar Cells, *Nature Materials*, in review, 2018.

[16] J. M. Cave, N. E. Courtier, I. A. Blakborn, T. W. Jones, D. Ghosh, K. F. Anderson, L. Lin, A. A. Dijkhoff, G. J. Wilson, K. Feron, J. M. Foster, G. Richardson and A. B. Walker. How to identify and fix losses from ion motion in perovskite solar cells. *Nature Communications*, in review, 2018.

[17] N. E. Courtier, J. M. Cave, J. M. Foster, A. B. Walker and G. Richardson. How transport layer properties affect perovskite solar cell performance: insights from a coupled charge transport/ion migration model. *Energy Env. Sci.*, accepted subject to minor revision, 2018.

[18] D. Ghosh, A. R. Smith, A. B. Walker, M. S. Islam. Mixed A-Cation Perovskites for Solar Cells: Atomic-Scale Insights Into Structural Distortion, Hydrogen Bonding, and Electronic Properties. *Chemistry of Materials*, 30:5194, 2018.

[19] O. J. Weber, D. Ghosh, S. Gaines, P. F. Henry, A. B. Walker, M. S. Islam, M. T. Weller. Phase Behavior and Polymorphism of Formamidinium Lead Iodide. *Chemistry of Materials*, 30:3768, 2018.

[20] S. Nagane, D. Ghosh, R. L. Z. Hoye, B. Zhao, S. Ahmad, A. B. Walker, M. S. Islam, S. Ogale and A. Sadhanala. Lead-Free Perovskite Semiconductors Based on Germanium-Tin Solid Solutions. *J. Phys. Chem. C*, 122:5940, 2018.

[21] S. Pering, W. Deng, J. R. Troughton, P. Kubiak, D. Ghosh, R. Niemann, F. Brivio, F. Jeffrey, A. B. Walker, M. S. Islam, T. Watson, P. Raithby, A. Johnson, S. E. Lewis, P. J. Cameron. Azetidinium lead iodide for perovskite solar cells. *J. Mater. Chem. A*, 520658-20665, 2017.

[22] D. Ghosh, P. Walsh Atkins, A. B. Walker, M. S. Islam, C. Eames. Good Vibrations: Locking of Octahedral Tilting in Mixed-Cation Iodide Perovskites for Solar Cells. *ACS Energy Lett.*, 2:2424, 2017.

[23] M. A. Carignano, A. Kachmar and J. Hutter. Thermal effects on CH3NH3PbI3 perovskite from ab initio molecular dynamics simulations. *J. Phys. Chem. C*, 119:8991, 2015.

[24] J. Hutter, M. Iannuzzi, F. Schiffmann and J. VandeVondele. CP2K: atomistic simulations of condensed matter systems. *Wiley Interdiscip. Rev. Comput. Mol. Sci.*, 4:15, 2014.

[25] P. Simon and Y. Gogotsi. Materials for electrochemical capacitors. *Nat. Mater.*, 7:845–854, 2008.

[26] J. Chmiola, G. Yushin, Y. Gogotsi, C. Portet, P. Simon, and P. L. Taberna. Anomalous increase in carbon capacitance at pore sizes less than 1 nanometer. *Science*, 313:1760–1763, 2006.

[27] E. Raymundo-Piñero, K. Kierzek, J. Machnikowski, and F. Béguin. Relationship between the nanoporous texture of activated carbons and their capacitance properties in different electrolytes. *Carbon*, 44:2498–2507, 2006.

[28] M. Salanne, B. Rotenberg, K. Naoi, K. Kaneko, P.-L. Taberna, C. P. Grey, B. Dunn, and P. Simon. Efficient storage mechanisms for building better supercapacitors. *Nat. Energy*, 1:16070, 2016.

[29] C. Largeot, C. Portet, J. Chmiola, P. L. Taberna, Y. Gogotsi, and P. Simon. Relation between the ion size and pore size for an electric double-layer capacitor. *J. Am. Chem. Soc.*, 130:2730–2731, 2008.

[30] S. Kondrat and A. A. Kornyshev. Superionic state in double-layer capacitors with nanoporous electrodes. *J. Phys.: Condens. Matter*, 23:022201, 2011.

[31] S. Kondrat, C. R. Perez, V. Presser, Y. Gogotsi, and A. A. Kornyshev. Effect of pore size and its dispersity on the energy storage in nanoporous supercapacitors. *Energy Environ. Sci.*, 5(4):6474–6479, 2012.

[32] D.-E. Jiang, Z. Jin, and J. Wu. Oscillation of capacitance inside nanopores. *Nano Lett.*, 11:5373–5377, 2011.

[33] G. Feng and P. T. Cummings. Supercapacitor capacitance exhibits oscillatory behavior as a function of nanopore size. *J. Phys. Chem. Lett.*, 2:2859–2864, 2011.

[34] D. T. L. Galhena, B. C. Bayer, S. Hofmann, and G. A. J. Amaratunga. Understanding capacitance variation in sub-nanometer pores by in-situ tuning of interlayer constrictions. *ACS Nano*, asap, 2016.

[35] N. Jäckel, P. Simon, Y. Gogotsi, and V. Presser. Increase in capacitance by subnanometer pores in carbon. *ACS Energy Lett.*, 1:1262–1265, 2016.

[36] J. C. Palmer, A. Llobet, S.-H. Yeon, J. E. Fisher, Y. Shi, Y. Gogotsi, and K. E. Gubbins. Modeling the structural evolution of carbide-derived carbons using quenched molecular dynamics. *Carbon*, 48:1116–1123, 2010.

[37] D. Roy and M. Maroncelli. An improved four-site ionic liquid model. *J. Phys. Chem. B*, 114:12629–12631, 2010.

[38] C. Merlet, B. Rotenberg, P. A. Madden, P.-L. Taberna, P. Simon, Y. Gogotsi, and M. Salanne. On the molecular origin of supercapacitance in nanoporous carbon electrodes. *Nat. Mater.*, 11:306–310, 2012.

[39] C. Merlet, M. Salanne, and B. Rotenberg. New coarse-grained models of imidazolium ionic liquids for bulk and interfacial molecular simulations. *J. Phys. Chem. C*, 116(14):7687–7693, 2012.

[40] S. K. Reed, O. J. Lanning, and P. A. Madden. Electrochemical interface between an ionic liquid and a model metallic electrode. *J. Chem. Phys.*, 126:084704, 2007.

[41] T. F. Willems, C. H. Rycroft, M. Kazi, J. C. Meza, and M. Haranczyk. Algorithms and tools for high-throughput geometry-based analysis of crystalline porous materials. *Microporous and Mesoporous Materials*, 149:134–141, 2012.

[42] R. L. Martin, B. Smit, and M. Haranczyk. Addressing challenges of identifying geometrically diverse sets of crystalline porous materials. *J. Chem. Inform. Model.*, 52:308–318, 2012.

[43] T. Mendez-Morales, M. Burbano, M. Haefele, B. Rotenberg, and M. Salanne. Ion–ion correlations across and between electrified graphene layers. *J. Chem. Phys.*, 148:193812, 2018.

[44] R. Burt, K. Breitsprecher, B. Daffos, P.-L. Taberna, P. Simon, G. Birkett, X. S. Zhao, C. Holm, and M. Salanne. Capacitance of nanoporous carbon-based supercapacitors is a trade-off between the concentration and the separability of the ions. *J. Phys. Chem. Lett.*, 7:4015–4021, 2016.

[45] A. Siria, P. Poncharal, A.-L. Biance, R. Fulcrand, X. Blase, S. T. Purcell, and L. Bocquet. Giant osmotic energy conversion measured in a single transmembrane boron nitride nanotube. *Nature*, 494:455–458, 2013.

[46] M. Simoncelli, N. Ganfoud, A. Sene, M. Haefele, B. Daffos, P.-L. Taberna, M. Salanne, P. Simon, and B. Rotenberg. Blue energy and desalination with nanoporous carbon electrodes: Capacitance from molecular simulations to continuous models. *Phys. Rev. X*, 8:021024, 2018.